RSC Sustainability

ROYAL SOCIETY OF CHEMISTRY

PAPER

View Article Online
View Journal | View Issue

Cite this: *RSC Sustainability*, 2024, **2**, 3916

The thermal behavior and pyrolysis mechanism of a polyimide gas separation membrane†

Qinxu Li,‡[a] Bo Chen,‡[b] Songyuan Yao,‡[a] Chao Sang,[a] Lu Lu,[c] Shilong Dong,[a] Hui Cao,[a] Zhihao Si *[a] and Peiyong Qin *[a]

Received 17th August 2024
Accepted 12th October 2024

DOI: 10.1039/d4su00489b

rsc.li/rscsus

Polyimide (PI) membranes have shown great advantages in gas separation due to their excellent thermal and chemical stability as well as high separation performance. With the increased demand for PI membranes, their recycling is a challenge for sustainable development. In this work, we systematically studied the pyrolysis behavior and performed kinetic analysis of a Kapton polyimide membrane, which has been suggested to exhibit a high gas separation performance. Results showed that the pyrolysis of the polyimide membrane was divided into three stages revealed by Py-GC/MS, with the main products being CO_2, CO, and H_2O. To study the pyrolysis kinetics of the polyimide in the main conversion range, the FWO, KAS, and Starink methods were adopted. The average activation energies were found to be 284.6, 286.1, and 286.5 kJ mol^{-1}, respectively. The pyrolysis of the polyimide membrane followed second-order (F2) and third-order (F3) models. Consequently, the pyrolysis technique provides valuable guidance for the recycling of polyimide membranes.

Sustainability spotlight

Aromatic polyimides are considered some of the most important membrane materials due to their flexibility, excellent thermal stability, and physical strength, and pyrolysis is an environmentally friendly method for processing waste polyimide membranes. This study delves into the sustainable recycling of polyimide membranes which are the most widely used membranes in gas separation. Through systematic pyrolysis, we demystified the decomposition into CO_2, CO, and H_2O to investigate the material's sustainability. Kinetic insights *via* the FWO, KAS, and Starink methods reveal activation energies guiding the polyimide's second and third-order breakdown, underscoring a circular approach to material reuse and waste reduction, resonating with global sustainability goals.

1. Introduction

With the implementation of green and sustainable development strategies, as well as the requirement for emission reduction and carbon sequestration, membrane separation technology has been developed and innovated to achieve energy savings, waste minimization and zero emissions.[1,2] Among different types of polymeric membranes, aromatic polyimides (PIs) showed high flexibility, great physical strength,[3] and high selectivity for gas separation. Fig. S1† shows the annual number of publications for the keywords "Polyimide" and "Membranes" between 2003 and 2023 from the Scopus database, and the increasing trend indicates that widespread attention has been paid to PI membranes. Furthermore, in 2012, the total PI membrane output reached 93 million m^2, approximately double the volume compared to 2008.[4] From 2019 to 2024, the PI membrane industry experienced a compound annual growth rate of 10%.[5] This trend suggests a sustainable increase in the demand for PIs. However, the advantageous characteristics also make PIs extremely difficult to decompose under natural conditions or to recycle.[6] Previous studies have explored solvent dissolution methods for decomposing PIs into monomers. The application of subcritical water has proven advantageous in enhancing PI hydrolysis.[7] Thomas *et al.* reported that atmospheric pressure conditions with an alkaline catalyst can also facilitate the hydrolysis of PIs.[8] Unfortunately, PIs with low purity often contain various impurities, which pose limitations on the reuse of solvents. Therefore, solvent dissolution is only suitable for high-purity PIs.

Pyrolysis, a thermochemical process, decomposes polymers into organic molecules without the use of solvents.[9] Pyrolysis is recognized for its environmentally friendly nature and minimal emissions.[10] Therefore, using pyrolysis to convert PI waste into high value-added chemical products is a highly suitable solution.[11] Notably, PIs contain significant quantities of volatiles,

[a]National Energy R&D Center for Biorefinery, College of Life Science and Technology, Beijing University of Chemical Technology, Beijing 100029, PR China. E-mail: zhsi@mail.buct.edu.cn; qinpeiyong@tsinghua.org.cn

[b]Systems, Power and Energy Research Division, James Watts School of Engineering, College of Science and Engineering, University of Glasgow, James Watt South, Glasgow G128QQ, UK

[c]Paris Curie Engineer School, Beijing University of Chemical Technology, Beijing 100029, PR China

† Electronic supplementary information (ESI) available. See DOI: https://doi.org/10.1039/d4su00489b

‡ These authors contributed equally to this paper.

rendering them a potential renewable energy resource and offering considerable economic advantages.[12,13] Currently, studies on the pyrolysis products, pathways and kinetics of aromatic PIs are still in progress. The results indicate that pyrolysis of aromatic PIs requires temperatures above 500 °C and produces CO, CO_2 and over 50 wt% charred solids.[14,15] The carbonized solids can be utilized as carbon precursors (*e.g.*, graphite membrane, activated carbon, and carbon foams).[16–18] Pan *et al.* found that aromatic PI foams had no residue in air, with pyrolysis yielding primarily CO_2, CO, and H_2O.[14] Hatori *et al.* found that during the initial stage of pyrolysis of PI membranes, bond cleavage and hydrogen transfer around the imide ring produced various intermediates in the aromatic portion of the polymer chain, proposing an early pyrolysis mechanism.[15] Ehlers *et al.* reported on the vacuum pyrolysis process of PIs, concluding that the isocyanate group was formed by the cleavage of the acyl ring between the carbonyl group and nitrogen in the main cleavage reaction.[19] Kessler *et al.* explored the thermal degradation mechanism and kinetics of PI membranes.[20] Isoconversional kinetic methods, which provide activation energy as a function of degradation, offer insight into the development of a five-step competitive and consecutive kinetic model. These findings suggest that PI pyrolysis exhibits significant potential for reclaiming PI waste. With an in-depth understanding of the pyrolysis products, pathways, and kinetics of PIs, it is possible to control the pyrolysis process and improve product yields. However, comprehensive studies on the pyrolysis process of PI materials are limited. Therefore, it is necessary to further elucidate the pyrolysis products, pathways, and kinetics in the pyrolysis process of PIs.

In this work, a Kapton PI membrane was selected to study the thermal behavior and pyrolysis mechanism. Kapton has high temperature resistance, great mechanical/chemical stability and no toxicity, while also having a rigid chain that is corrosion resistant, insoluble, and non-melting. Thus, it is suitable for separating highly soluble gases such as CO_2, alkanes, olefins, *etc.*[6] The chemical structure, elemental composition, microstructure, morphology and thermodynamic characteristics of the PI membrane were investigated using Fourier transform infrared spectroscopy (FT-IR), elemental analysis (EA), X-ray photoelectron spectroscopy (XPS), X-ray crystallography (XRD), Raman spectroscopy, scanning electron microscopy (SEM), and thermogravimetric analysis (TGA). Meanwhile, the gas separation ability of the PI membrane was evaluated using pure H_2, CO_2, CH_4, N_2, and O_2 as test gases. Then, the decomposition stage characteristics of the PI membrane were systematically investigated by thermogravimetry-differential thermogravimetry (TG-DTG). The pyrolysis behavior, products and pathways of the PI membrane in a nitrogen atmosphere were investigated by Py-GC/MS and TG-IR. The results provide a foundation for practical applications. Finally, the Flynn–Wall–Ozawa (FWO), Kissinger–Akahira–Sunose (KAS) and Starink methods were employed to calculate the activation energy of PI membrane pyrolysis. The master-plot method was used to determine the reaction model of the pyrolysis process of the PI membrane, which could further unveil the reaction mechanism of PI membrane pyrolysis.

2. Experimental section

2.1 Materials

PAA/NMP solution (15 wt%) was purchased from Changzhou Runge Chemical Materials Co., Ltd, China. Isopropanol (99.5%) and *n*-hexane (99%) were obtained from Shanghai Macklin Co., Ltd, China. Anhydrous methanol (99.5%) was purchased from Shanghai Aladdin Biochemical Technology Co., Ltd.

2.2 Preparation of the membrane

10 g of PAA/NMP solution was added into a 25 ml beaker and sealed for 24 h to eliminate blisters. It was moved into an oven and heated at 60 °C for 2 h, then applied to a glass plate using an automatic coater (Elcometer 4340, UK). Then, the membrane was transferred into a water/methanol (1 : 1) solution for 24 h. After that, the membrane was transferred to *n*-hexane for 10 min and then to isopropanol for 10 min, respectively, repeating these processes three times. Finally, the membrane was dried and transferred to a tube furnace for the thermal imidization process. The heating program of the tube furnace is shown in Fig. S2.†

2.3 Membrane characteristics

A Jeol-JSM-IT800 (HL) instrument was used to observe the SEM images. XRD data were obtained using a Bruker D8 Advance instrument (5–60°, 5° min^{-1}). FT-IR spectroscopy of the PI membrane, in the range of 400–4000 cm^{-1}, was conducted using a Nicolet iS50 device. The XPS spectra and the elemental compositions of the PI membrane (0.5 × 0.5 cm^2) were obtained using an ESCALAB 250Xi device. Raman spectroscopy of the PI membrane (1 × 1 cm^2) was conducted using a Raman instrument at a wavenumber of 514 nm (Horiba-LabRAM HR evolution, JP). The contents of C, H, O, and N in the PI membrane (1 × 1 cm^2) were analyzed using an elemental analyzer (EA, Elementar-UNICUBE, GER).

2.4 Thermogravimetric analysis

The thermal decomposition of the prepared PI membrane was detected using a thermogravimetric analyzer (TGA, NETZSCH-STA449F3, GER). Test conditions: temperature (room temperature-1000 °C), heating rate (5, 10, 20, and 30 °C min^{-1}) and N_2 (60 ml min^{-1}).

2.5 Product analysis

The functional groups of all volatile products of the samples were observed using TG-IR (TG, NETZSCH-STA449F3, GER; FT-IR, Nicolet iS20, USA; NETZSCH-QMS 403, GER) devices. Test conditions: PI membrane area (1 × 1 cm^2), temperature (room temperature-1000 °C), heating rate (10 °C min^{-1}), and N_2 (60 ml min^{-1}). TG-IR transmission line temperature (300 °C), FT-IR resolution 4 cm^{-1}, 16 s. Furthermore, the PY-GC/MS (Frontier-EGA/PY3030D, JP; Thermo Fisher-TRACE1310, USA; Thermo

Fisher-ISQ7610, USA) test conditions were as follows: PI membrane area (1×1 cm^2), pyrolysis temperature (600 °C), and ramp rate (10 °C min^{-1}).

2.6 Gas permeation and selectivity

This study utilized a custom-built constant volume/variance pressure instrument (FHMPermcellLab), focusing on H_2, N_2, O_2, CO_2, and CH_4 gas permeation. Feed pressure: 1 bar. Test temperature: 25 °C. Prior to the test, the instrument was fully purged, followed by a steady-state gas flow into the upstream permeation zone. The ideal selectivity was obtained in this work, and the downstream pressure changes over time (dp/dt) were used to quantify molar flux. The permeability (P_i) to gas i was determined as follows:[21]

$$P_i = \frac{273V}{760AT\left(\frac{P_2}{P_1}\right)}\frac{dp}{dt} \quad (1)$$

where V, A, and T represent the downstream chamber volume (cm^3), system temperature (K), and effective membrane area (m^2), respectively. P_1 and P_2 represent the atmosphere (psia) and the upstream pressure (psia), respectively. The permeability (P_i) was calculated in Gas Permeation Unit (GPU). The selectivity was calculated as follows:

$$\alpha_{i/j} = \frac{P_i}{P_j} \quad (2)$$

where P_i and P_j represent the permeability of gas i and gas j, respectively.

2.7 Kinetics analysis

In the non-isothermal process, the kinetic equation for the decomposition rate was calculated as follows:[22]

$$\frac{d\alpha}{dt} = k(T)f(\alpha) \quad (3)$$

$$\alpha = \frac{m_t - m_0}{m_f - m_0} \quad (4)$$

The Arrhenius equation adequately represents the rate constant:[20]

$$K(T) = A\,e^{-E/RT} \quad (5)$$

Substituting eqn (5) into (3), the following equation is obtained:

$$\frac{d\alpha}{dT} = \frac{A}{\beta}f(\alpha)e^{-E/RT} \quad (6)$$

A linear transformation of eqn (6) and integration yields the following integral expression with respect to $f(\alpha)$:

$$G(\alpha) = \int_0^\alpha \frac{d\alpha}{f(\alpha)} = \frac{A}{\beta}\int_{T_0}^{T} e^{-E/RT}dT \approx \frac{A}{\beta}\int_0^T e^{-E/RT}dT \quad (7)$$

The KAS, FWO, and Starink methods were selected for calculating E_a due to their robustness, reliability, and accuracy. These methods offer the advantage of not requiring in-depth knowledge of the reaction mechanism, thereby minimizing errors in E_a estimation. The KAS and FWO methods are particularly valued for their simplicity and widespread acceptance, while the Starink method is known for its improved accuracy and versatility. The equations of the KAS, FWO and Starink methods are detailed in Table S1.†[23–25]

Based on the E_a calculated by the three methods, the master-plot method defined the PI membrane pyrolysis model. The exponential integral $P(u)$ of the temperature is shown as follows:[26]

$$P(u) = \frac{\exp(-u)}{u(1.00198882 + 1.87391198)} \quad (8)$$

$$u = \frac{E}{RT} \quad (9)$$

Transforming eqn (7) and selecting conversion rate (α) = 0.5 as the reference point, the expression is obtained as follows:

$$G(0.5) = \frac{ARP(u_{0.5})}{\beta R} \quad (10)$$

$$u = \frac{E}{RT_{0.5}} \quad (11)$$

Combining eqn (8) and (10), the integral expression for the master-plot is obtained as follows:

$$\frac{G(\alpha)}{G(0.5)} = \frac{P(u)}{P(u_{0.5})} \quad (12)$$

The thermodynamic parameters are obtained as follows:

$$A = -\frac{\beta E_a}{RT_m{}^2 f'(\alpha_m)}\exp\left(\frac{E_a}{RT_m}\right) \quad (13)$$

$$\Delta H = E - RT \quad (14)$$

$$\Delta G = E_a + RT_m \ln(K_b T_m/hA) \quad (15)$$

$$\Delta S = (\Delta H - \Delta G)/T_m \quad (16)$$

Table S2† presents the detailed descriptions and units of all variables utilized in the provided equations.

3. Results and discussion

3.1 Membrane characteristics

Fig. 1a illustrates the FT-IR spectrum of the PI membrane. The symmetric and antisymmetric stretching vibrations of the two C=O groups in the imide ring are observed at 1775 cm^{-1} and 1715 cm^{-1}, respectively.[27,28] The stretching vibration of the C–N bond is observed at 1370 cm^{-1}. Additionally, the deformation or angular vibration of C=O is observed at 723 cm^{-1}.[29] According

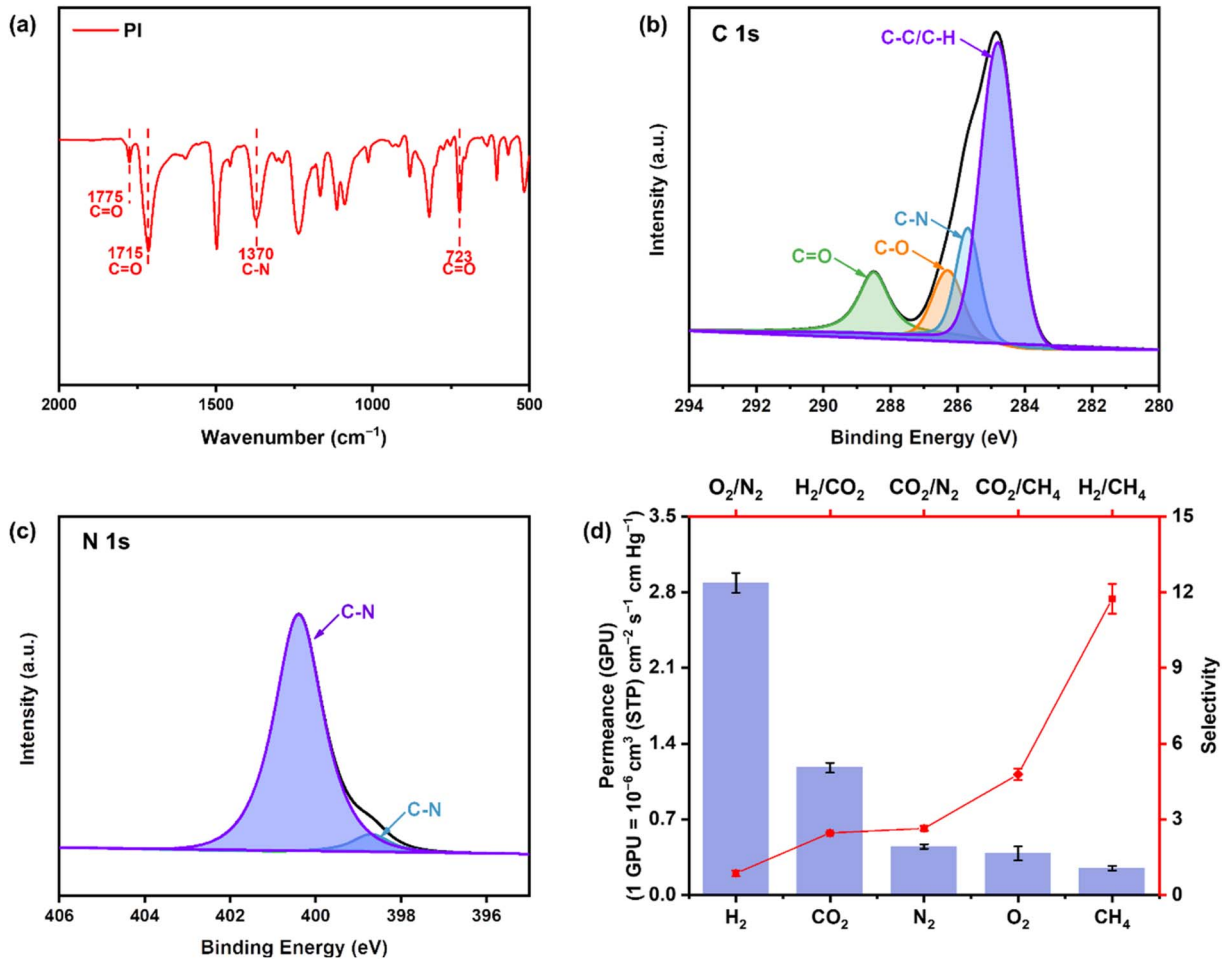

Fig. 1 (a) FT-IR, (b) C 1s and (c) N 1s spectra of the PI membrane; (d) gas permeance and selectivity of the PI membrane.

to previous XRD analysis, the crystalline structure of PI is an orthorhombic crystal lattice.[30] Fig. S3a† shows the XRD pattern of the PI membrane, revealing two broad amorphous peaks at 5.80° and 17.80°, corresponding to the (002) and (110) diffraction indices, respectively.[31] This indicates that the polymer chains parallel to the membrane plane are regular and ordered to some extent.[29,32] Fig. S3b† displays two significant characteristic peaks at 1389 cm^{-1} and 1785 cm^{-1}, related to the C=O group and the C–C bond in the benzene ring, respectively.[32] The imide group peak exhibits greater intensity compared to the benzene ring peak, which is attributed to the larger scattering cross-sectional area of the imide group in Raman scattering.[33] These findings validate the successful synthesis of PI membranes through heat crosslinking with PAA. The XPS spectra obtained from the membrane samples are shown in Fig. 1. In Fig. 1b, four different carbon species were identified. The peaks at 284.8, 285.7, 286.3, and 288.5 eV correspond to carbon atoms not directly attached to the imide ring, the nitrogen-bonded carbon atoms (C–N), the C–O bond of the ether groups, and the C=O bond of the imine ring, respectively.[9,34,35] In Fig. S4,† the O 1s peaks at 532 and 533.5 eV represent the C=O bond of the imine ring and the C–O bond of the ether group.[36] In Fig. 1c, the N 1s peaks at 400.4 and 398.6 eV correspond to the Kapton-type C–N and pyridine-type C–N bond, respectively.[37] Consistent with previous studies, the results indicate that the PI membrane exhibits characteristics typical of Kapton-type polyimides.[34,38] Fig. S5† presents the SEM images of the PI membrane, showing crystalline microspheres on the surface, likely resulting from the uneven distribution of polymers with different molecular weights during the membrane preparation process. The accumulation of tiny spherical particles on the membrane surface also contributes to increased surface roughness.[39,40] The cross-section of the membrane shows a spongy layer structure with uniform membrane thickness distribution.[41] Moreover, the membrane has a distinct skin layer, which contributes to enhanced gas selectivity.[42] Table S4† shows the results of XPS spectroscopy, which reveal the surface elemental composition and valence structure of PI membranes. The elemental composition of the PI membrane, determined using an elemental analyzer, is also listed in Table S4.† Notably, elemental carbon (C) is the major component of the PI membrane, accounting for 68.52 wt% of the composition. This suggests that the polymer membrane can be used as a sustainable carbon source during the pyrolysis process. The PI membrane contains a small amount of N, which minimizes the release of NO_x in the pyrolysis recovery process.

All elements positively contribute to the thermochemical conversion of the PI membrane.[43] Fig. 1d presents the gas permeance and selectivity of the PI membrane. Compared to previous studies, the membrane exhibits slightly lower permeability for all gas types.[41,44,45] This is attributed to the spongy cross-sectional morphology and the presence of a modest skin layer, which enhances resistance to gas molecule transport, resulting in low permeability (Fig. S4†).[46] Among these gases, H_2 has the highest permeability of 2.88 CPU, while CH_4 has the lowest permeability of 0.25 GPU. This is attributed to the smaller molecular dynamics radius of H_2, resulting in the least resistance to mass transfer.[47] Conversely, CO_2 and CH_4, with much larger molecular kinetic radii than H_2, exhibit lower permeability.[48] The membrane exhibited the highest H_2/CH_4 selectivity, which is attributed to fewer defects on the membrane surface and the increased molecular sieving action of the epidermal layer, which facilitates the interception of larger molecular gases.[49]

3.2 Thermogravimetric analysis

The TGA-DTG curves of the PI membrane are shown in Fig. 2. The pyrolysis of the PI membrane is divided into Y_1, Y_2 and Y_3 stages. The first stage (Y_1) of pyrolysis is mainly attributed to the evaporation of H_2O and CO_2 within the PI membrane. The second stage (Y_2) represents the principal stage of the PI membrane pyrolysis process. The last pyrolysis zone (Y_3) corresponds to char devolatilization or decomposition. According to the DTG curves of PI at different heating rates, the PI membrane was decomposed with one sharp peak which indicated that the PI membrane decomposed in one step. Moreover, as the heating rate rises, the T_m gradually increases; the increase of T_m is related to the amplified heat flux stemming from the elevated heating rate.[50] Table S5† shows the characteristic parameters of the TGA-DTG curves of the PI membrane. As the heating rate rises, the quantity of volatiles undergoes an increase. This phenomenon can be attributed to the intensified generation of heat fluxes, which reduces the viscosity of the decomposed samples. Additionally, the increased heat flux enhances the efficiency of heat transfer between the sample's surroundings and its internal molecular composition, thereby facilitating the decomposition of organic constituents within the tested samples.[51]

3.3 Product analysis by TG-IR

The TG-IR coupling method was used to further explore the pyrolysis products of the PI membrane. The 3D FT-IR and 2D FT-IR mapping data were constructed for analyzing the gas products, as shown in Fig. 3. From room temperature to 540 °C, only small amounts of H_2O and CO_2 were detected, corresponding to the first stage (Y_1). From 540 to 690 °C, the second stage (Y_2) of pyrolysis occurs, representing the main phase of PI pyrolysis. This stage yields abundant volatile compounds. The peaks within 3400–3900 cm^{-1} represent the free –OH, gaseous H_2O, and C–H bond.[20,52] The strongest peaks appear in the 2000–2500 cm^{-1} range, with peaks at 2352 and 666, and 2177 and 2106 cm^{-1} corresponding to CO_2 and CO, respectively.[13,53] At 1000–2000 cm^{-1}, the characteristic peak of NO_x and the variable angle vibration peak of water are located at 1300–1900 cm^{-1}.[20] The C–C skeleton vibration peaks of the benzene ring are at 1600, 1580, 1500, and 1450 cm^{-1}.[53] The vibration of the N–H bond is at 1240 cm^{-1},[54] and the double bands of $-NH_2$ are at 963 and 927 cm^{-1}.[14] Peaks within 500–1000 cm^{-1} include the vibration of nitro and nitroso compounds at 745 cm^{-1}.[55] From 690 to 1000 °C, the third stage (Y_3) occurs, with peaks in the 3400–3900 and 1200–1900 cm^{-1} range persisting. These peaks correspond to the vibration of free –OH, H_2O, C–H, NO_x, and the benzene ring skeleton. However, the characteristic peaks of CO_2 and CO disappear, indicating that the imide ring in PI has been completely cleaved in the second stage (Y_2). The results show that the main pyrolysis processes of the third stage (Y_3) may be as follows: (1) the pyrolysis of aromatic compounds such as phenol, aniline and benzonitrile to produce free –OH, H_2O, NO_x, and benzene. (2) The aggregation of benzene rings to form polycyclic aromatic compounds (*e.g.*, naphthalene and

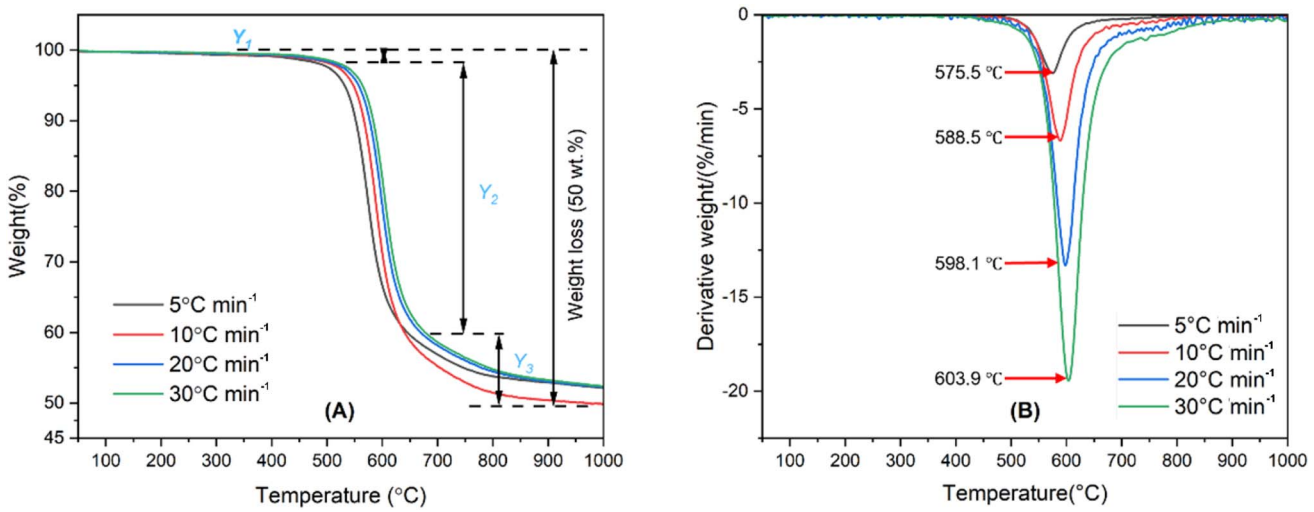

Fig. 2 The TGA-DTG curves of the PI membrane under varying heating rates.

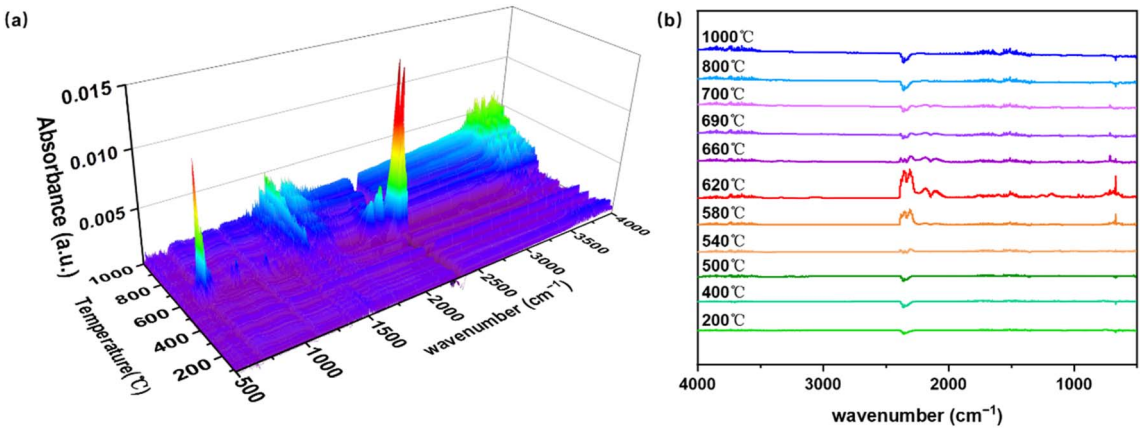

Fig. 3 (a) 3D FT-IR and (b) 2D FT-IR mapping data of the TG exit gas at a 10 K min^{-1} heating rate at the onset of pyrolysis.

fluoranthene).[56] (3) The cleavage of the ring structure of aromatic compounds to generate long-chain alkane compounds. (4) The graphitization of the PI membrane.[57] Some diatomic molecules, such as H on the benzene ring, N on the imine ring, N_2, and O_2, cannot be identified by FT-IR. These results align with previous PI membrane pyrolysis mechanisms, confirming that CO_2, CO, and H_2O are the main gaseous products.[9,54,58–60] The main sources of CO_2 are as follows: (1) the production of isocyanate groups and CO through the pyrolysis of the imide ring, with CO_2 resulting from the hydrolysis of isocyanate groups.[15] (2) Decarboxylation of acid end groups or uncyclized amic acids.[53] (3) Hydrolysis of the imide ring and decarboxylation.[9] The release of N-containing elemental compounds is related to the C–N cleavage of the imide ring. The above three points are further confirmed in PI membrane pyrolysis mechanisms (Fig. 4–7).

3.4 Product analysis by Py-GC/MS

According to thermogravimetric analysis, PI reaches its maximum pyrolysis rate at a temperature of 588.5 °C. In the lower temperature range (room temperature-540 °C), the main products are CO_2 and H_2O. Zhu *et al.*'s investigation into the pyrolysis of PI under vacuum conditions supports these findings, noting that CO_2 and H_2O are the main products in the lower temperature range along with varying amounts of carbon monoxide.[61] This is consistent with the findings of Ehlers *et al.* Considering the energy consumption during the pyrolysis of PI membranes, the maximum pyrolysis temperature was set at 600 °C.[19] The distribution of the pyrolysis products of the PI membrane at 600 °C is shown in Table S6.† Among these pyrolysis products, CO_2 and O_2 had the highest content, with CO not detected. It is possible that during the pyrolysis process, CO further reacted with O_2 in the thermal environment to form CO_2. Aromatic volatiles such as phenol, aniline, benzonitrile, 4-phenoxyaniline and dibenzofuran aromatic volatiles were detected in higher amounts. Isomeric compounds such as 1,4-dicyanobenzene and 1,3-dicyanobenzene exhibited a 1 : 1 content ratio. Similarly, 2-cyanobenzoic acid and phthalimide were found in a 1 : 1 isomeric ratio.[62] Small quantities of phenyl isocyanate, *p*-aminophenol, 2-dibenzofuranamine, 4,4′-diaminodiphenyl ether, and diphenyl ether were also detected. It is noteworthy that the pyrolysis products also included two components with molecular structures similar to that of a PI monomer. The long molecular chains decomposed into short chains or intermediates, and then into low molecular weight compounds.[9] A similar phenomenon was also found in the study by Kessler *et al.*[20] Based on the above results, Fig. 4–7 propose a complex multistage pyrolysis pathway for PI.

3.5 Mechanism of membrane pyrolysis

As shown in route A (Fig. 4), part of the imide ring retains its stability at 600 °C. Cleavage occurs at the C–N bond between the imide ring and the diphenyl ether, yielding an imide ring free radical and a diphenyl ether free radical portion.[15] The reaction of the diphenyl ether free radical with a H atom produces intermediate I (orange arrow). And the imide ring free radicals undergo molecular rearrangement and decarboxylation to produce benzonitrile, 1,4-dicyanobenzene and 1,3-dicyanobenzene (red arrow).[19] However, another mechanism has been proposed by Żurakowska-Orszàgh *et al.* in which imide ring free radicals can be converted to benzoylisocyanate, forming a cyano group.[59] Route B describes the pathway for the imide ring cleavage. The imide rings is cleaved at 600 °C to produce an intermediate containing an isocyanate group (orange arrow), intermediate IV and CO (purple arrow). This mechanism of pyrolysis of the isocyanate group is the same as that proposed by Ehlers *et al.*[19] The intermediate containing an isocyanate group can be hydrolyzed in one of three ways to produce intermediate II and CO_2 (orange arrow). The outcomes of the other two pathways depend on how the ether bond is cleaved. When the ether bond is fully cleaved, the free radicals react with hydrogen to form phenyl isocyanate and benzene, with the possibility of forming O_2 or H_2O (green arrow).[63] Phenyl isocyanate is further hydrolyzed to form aniline and CO_2. The ether bond cleavage follows the same mechanism as previously demonstrated by Ehlers *et al.* for diphenyl ether pyrolysis.[64] When the ether bond is partially cleaved, the free radicals react with H to form phenyl isocyanate and phenol (red arrow). Similarly, the phenyl

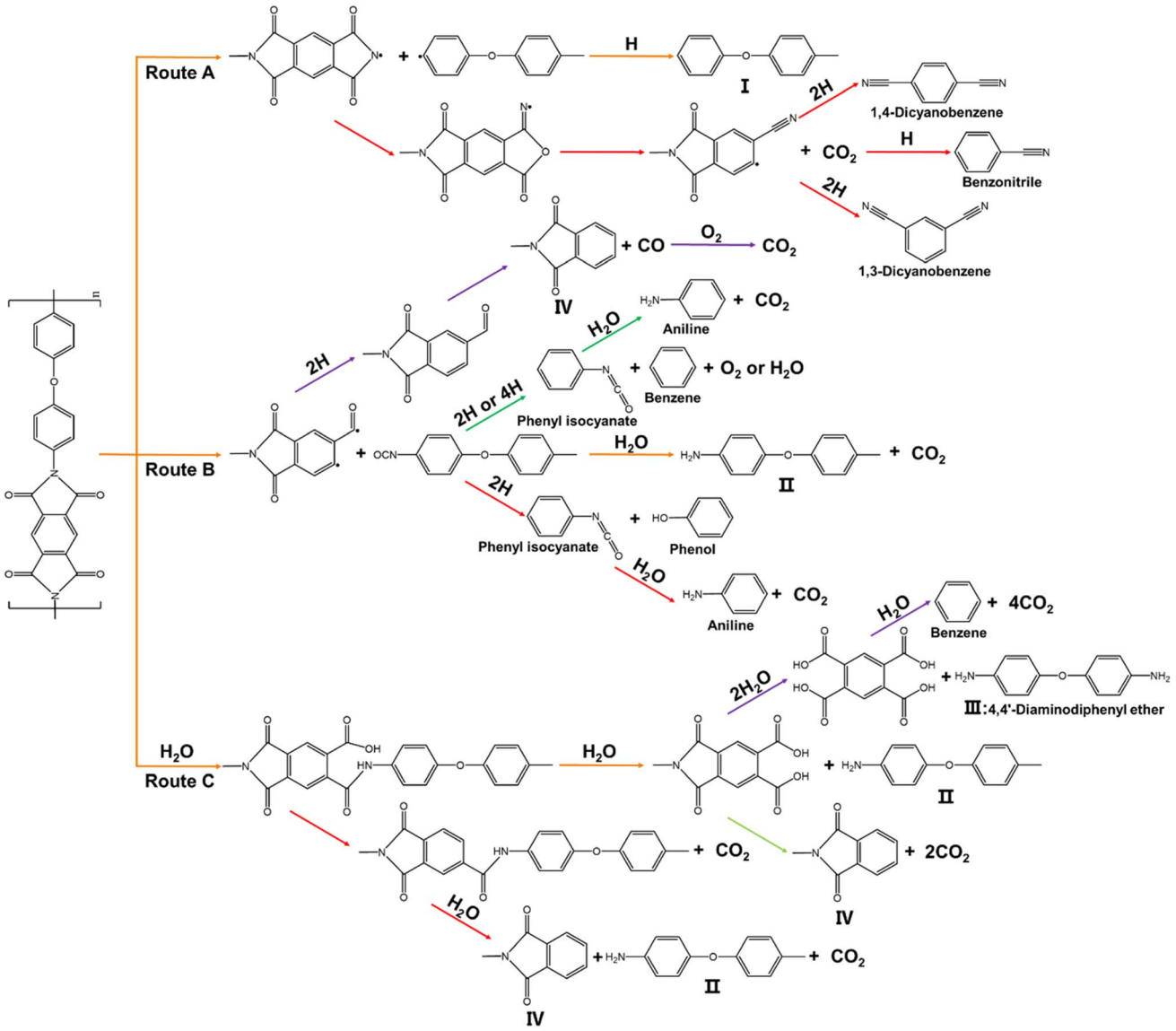

Fig. 4 Three pyrolysis reaction pathways for PI (routes A, B and C).

isocyanate is further hydrolyzed to form aniline and CO_2.[15] In route C, the imide rings are hydrolyzed but not pyrolysed due to the presence of a small amount of water in the sample and the water generated during pyrolysis.[9] Two carboxyl groups and intermediate II are produced after hydrolysis of the one-sided imide ring of the benzene ring (orange arrow). The carboxyl group is decarboxylated at high temperature to produce CO_2 and intermediate IV (light green arrow). In the other case, the carboxyl group from the first hydrolysis is immediately decarboxylated to produce CO_2, and then the process of hydrolytic decarboxylation is repeated to produce intermediates II and IV, and CO_2 (red arrow). Four hydrolyses on both sides of the benzene ring produce benzenetetracarboxylic acid and intermediate III (4,4′-diaminodiphenylether) (purple arrow). Benzenetetracarboxylic acid is decarboxylated by pyrolysis to produce benzene and CO_2.[58]

Fig. 5 shows the pyrolysis pathways of intermediates I, II, and III. Since intermediates I, II, and III all contain ether bonds, the pyrolysis pathways are somewhat related. Cleavage occurs at the C–N bond; intermediate I generates diphenyl ether and intermediate II generates 4-phenoxyaniline.[15] When the imide ring is cleaved, intermediate I generates 4-phenoxyaniline and intermediate II generates 4,4′-diaminodiphenylether (intermediate III). According to the different pathways of ether bond cleavage, diphenyl ether, 4-phenoxyaniline and 4,4′-diaminodiphenylether (intermediate III) are cleaved to phenol, aniline, benzene, and *p*-aminophenol. This is accompanied by O_2 or H_2O production.[19]

The pyrolysis pathway of intermediate IV is shown in Fig. 6. Since cleavage occurs at the C–N bond, the phthalimide free radical is produced.[15] On the one hand, the phthalimide free radical undergoes molecular rearrangement and pyrolytic decarboxylation to form benzonitrile and CO_2 (purple arrow).[59]

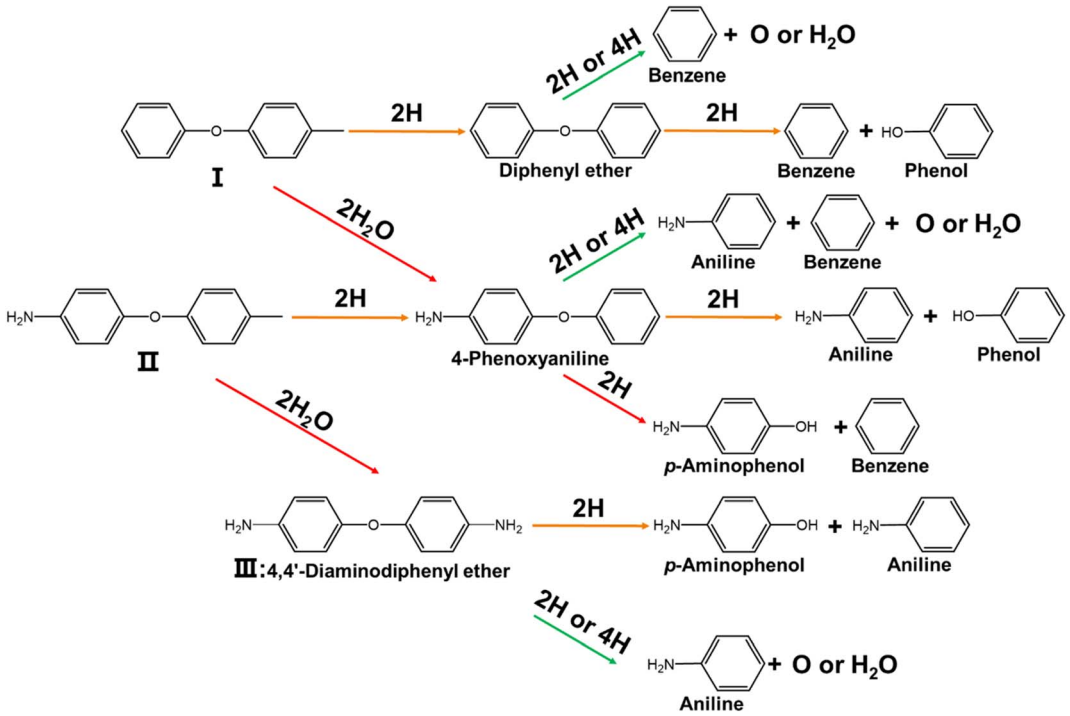

Fig. 5 The pyrolysis reaction pathways of intermediates I, II and III.

On the other hand, the phthalimide free radical reacts with H to form phthalimide, which is then hydrolyzed to form phthalic acid. Phthalic acid is pyrolytically decarboxylated to benzene and CO_2 (blue arrow).[58] When the ether bond is cleaved, it yields benzene, phenol and phthalimide radicals according to the cleavage position of the ether bond.[19] Phthalimide continues to participate in the previous pyrolysis pathway.

The main source of H atoms during pyrolysis is the benzene ring in the diphenyl ether fraction.[15] As shown in Fig. 7, the free radical component generated during the pyrolysis process extracts hydrogen atoms from the diphenyl ether portion. The diphenyl ether free radical intermediates can generate dibenzofuran and 2-dibenzofuranamine *via* molecular coupling reactions. 2,8-diaminodibenzofuran was not detected, implying

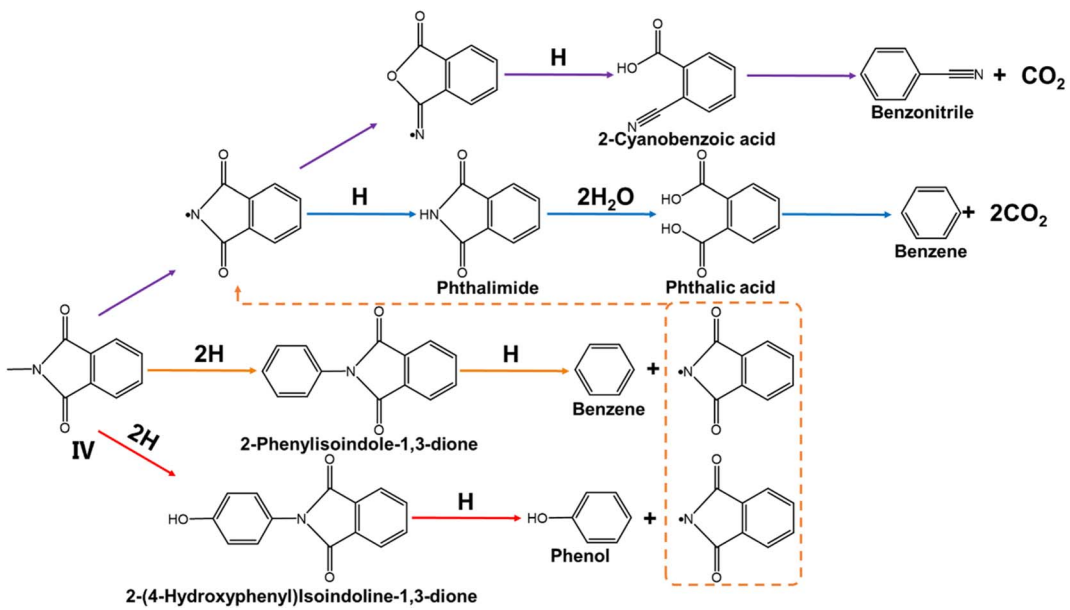

Fig. 6 The pyrolysis reaction pathway of intermediate IV.

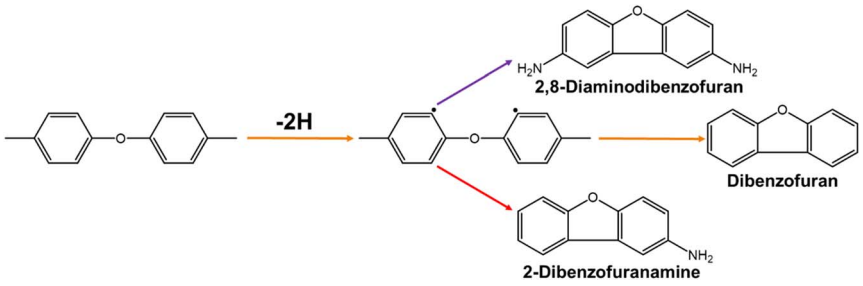

Fig. 7 The main source of H atoms during pyrolysis.

that a potential pyrolysis pathway (purple arrow) involves 2,8-diaminodibenzofuran.

3.6 Kinetics analysis

3.6.1 Activation energy calculation. Fig. 8a–c display the linear plots for E_a determination of the PI membrane by the FWO, KAS and Starink methods. Notably, these lines maintain parallelism in most α ranges, particularly within the α of 0.1–0.7. Nevertheless, it's worth noting that some of these fitted lines deviate from being parallel, which is due to the presence of numerous concurrent reactions and unstable radical interactions observed simultaneously.[65] These factors result in an elevated complexity in the pyrolysis mechanism, particularly noticeable at both lower and higher α ranges. Fig. 8d illustrates the E_a for PI membrane pyrolysis at different α. The E_a values demonstrates a noticeable increasing trend within the α of 0.1–0.5. There's a rapid increase within the α of 0.1–0.2; this phenomenon could be attributed to the scission initiation of linkages, such as dehydration and the onset of depolymerisation.[65] The E_a values stabilize within the α of 0.2–0.7. During this interval, the primary polymer main chain decomposed and some unstable reaction products were probably generated.[66,67] A marked decline in the E_a value is observed within the α of 0.7–0.9. This reduction is related to the depletion of most volatiles in the PI membrane. Consequently, less energy is needed for the occurrence of the pyrolysis reaction.[68] Table S7† lists the E_a and linear correlation coefficients calculated by the three methods. The E_a value calculated by the Starink (286.5 kJ mol^{-1}) method slightly surpasses those derived from the FWO (284.6 kJ mol^{-1}) and KAS (286.1 kJ mol^{-1}) methods. Differences in the derivation methodology and error range between models may explain this disparity.[69] There is a notable decrease in prediction accuracy at the α of 0.9 in all methods. Within the α of 0.1–0.8, all three

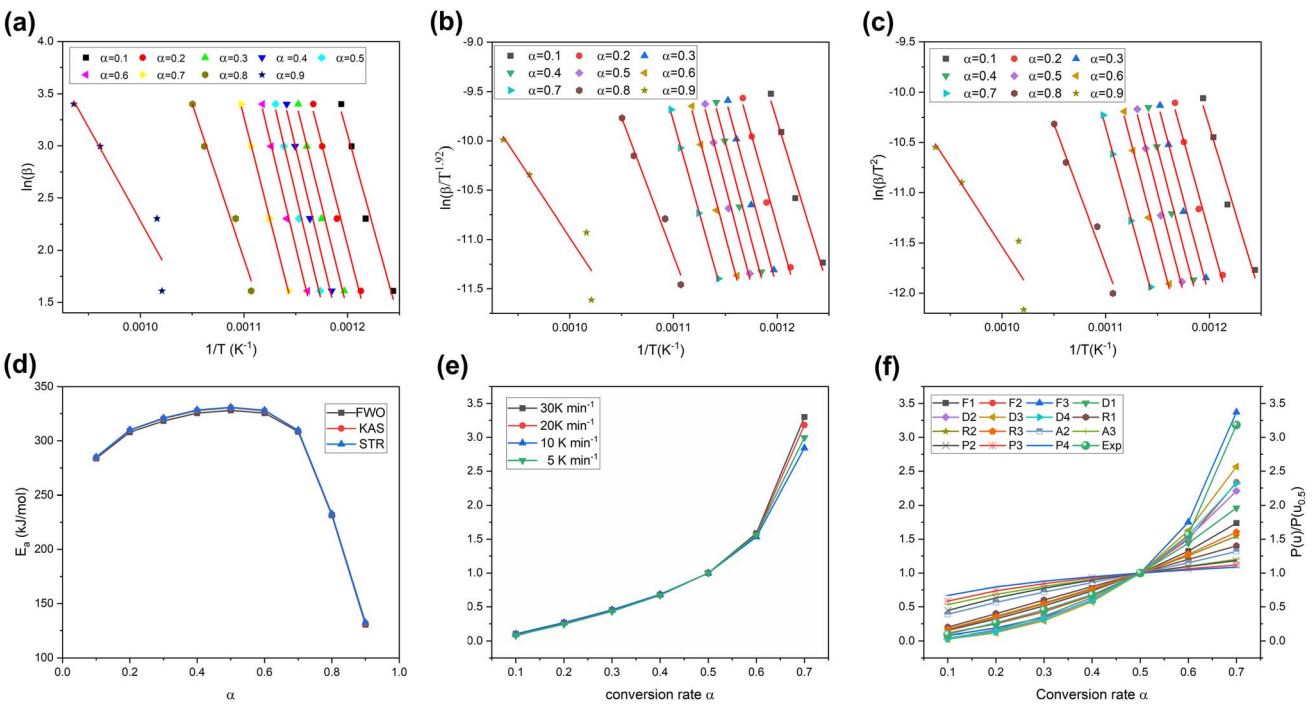

Fig. 8 The linear plots for E_a determination of the PI membrane: (a) FWO, (b) KAS and (c) Starink methods; (d) the E_a of PI membrane pyrolysis at different α; (e) the curves of experimental master-plots $P(u)/P(u_{0.5})$; (f) the comparison of the experimental $P(u)/P(u_{0.5})$ and master plots $G(\alpha)/G(0.5)$ of the PI membrane at 10 K min^{-1}.

methods demonstrate robust predictive capabilities, with R^2 values exceeding 0.97. This phenomenon agrees well with findings in the existing literature, which demonstrates that FWO, KAS and Starink are equal conversion methods suitable for E_a calculation in the main decomposition range, while they may give some significant errors in lower and higher α regions.[70]

3.6.2 Assessment of thermodynamic parameters. In large-scale pyrolysis processes, the optimization of the pyrolysis reactor largely depends on thermodynamic parameters.[71] These essential parameters including the A, ΔH, ΔG and ΔS were calculated using eqn (13)–(16), employing the E_a values, and the results are presented in Table S7.† ΔH represents the energy involved in the cleavage of old bonds and the formation of new bonds.[72] The positive ΔH values across all α regions indicate the pyrolysis process of the PI membrane has an endothermic nature.[69] Comparing E_a with ΔH, the variation of ΔH is consistent with E_a, reflecting the changes in heat/energy during the pyrolysis of the PI membrane. It should be noted that the increasing ΔH not only indicates that more energy is required for breaking chemical bonds, but also that there is more energy consumption for transforming the disorder structures into organized ones. ΔG signifies the total energy transformation for the formation of the activated complex.[68] The ΔG values of PI membrane pyrolysis are positive and high, which reveals that the pyrolysis of the PI membrane is non-spontaneous and a significant amount of energy is required for the occurrence of the pyrolysis reaction. ΔS represents the randomicity or disorder degree of a system.[73] As shown in Table S8,† the ΔS values within the α of 0.1–0.7 are positive, indicating that the degree of disorder in the system is gradually increasing, while the negative ΔS at the end of the pyrolysis reaction reveals a distinct molecular arrangement and an increased orderliness of the pyrolysis reaction. In addition, the increasing ΔS within the α of 0.1–0.5 shows that the PI membrane pyrolysis reaction was far from thermodynamic equilibrium at this stage, indicating that the reaction reactivity was high and the formation of an activated complex was more rapid.[74]

3.6.3 Kinetics model analysis of PI pyrolysis. In the current study, the pyrolysis reaction model for the PI membrane was ascertained using the master-plot method, which can further explain the kinetic mechanism of PI membrane pyrolysis. The determination of the pyrolysis reaction model is crucial as it offers insights that can help in the selection of suitable reactors and the optimization of reactor design.[75] Fig. 8e shows the experimental master-plots $P(u)/P(u_{0.5})$ of the PI membrane. The trend of each curve remains almost the same. This illustrates the pyrolysis of the PI membrane adheres to a singular kinetic model.[76] Fig. 8f shows a comparison between the theoretical master-plots $G(\alpha)/G(0.5)$ and the experimental master-plots $P(u)/P(u_{0.5})$ of PI membrane pyrolysis (Table S3†). Within the α of 0.1–0.6, the PI membrane pyrolysis reaction follows the second-order model (F2). However, the third-order model (F3) fits best for the α range of 0.6–0.7. The change in the reaction model from F2 to F3 can be attributed to the high thermal stability at higher α.[75]

4. Conclusions

This study investigated the preparation, gas separation performance, pyrolysis behavior and kinetics of the Kapton PI membrane in a nitrogen environment. The TGA results showed that the decomposition of the PI membrane was divided into three stages. The results from TG-IR and Py-GC/MS suggested the main products during the pyrolysis of PI membranes were CO_2, CO, and H_2O. The multistage pyrolysis pathway of the PI membrane was unveiled according to the Py-GC/MS results. The kinetics study of the PI membrane revealed that the FWO, KAS and Starink methods are optimal for calculating E_a in the main decomposition range. The reaction model of PI membrane pyrolysis followed the second-order (F2) and third-order (F3) reaction models, which was determined by the master-plot method. These findings suggest that pyrolysis is a promising method to treat end-of-life polyimide membranes.

Data availability

Data will be made available on request.

Conflicts of interest

There are no conflicts of interest to declare.

Acknowledgements

This work was funded by the National Natural Science Foundation of China (22278023, 22208010), Beijing Natural Science Foundation (2222015), and the long-term funding from the Ministry of Finance and the Ministry of Education of PRC.

References

1 A. Yusuf, A. Sodiq, A. Giwa, J. Eke, O. Pikuda, G. De Luca, J. L. Di Salvo and S. Chakraborty, A review of emerging trends in membrane science and technology for sustainable water treatment, *J. Cleaner Prod.*, 2020, **266**, 121867.

2 M. M. Abdel-Mottaleb, A. Khalil, S. Karim, T. A. Osman and A. Khattab, High performance of PAN/GO-ZnO composite nanofibers for photocatalytic degradation under visible irradiation, *J. Mech. Behav. Biomed. Mater.*, 2019, **96**, 118–124.

3 H. Sanaeepur, A. Ebadi Amooghin, S. Bandehali, A. Moghadassi, T. Matsuura and B. Van Der Bruggen, Polyimides in membrane gas separation: Monomer's molecular design and structural engineering, *Prog. Polym. Sci.*, 2019, **91**, 80–125.

4 S. Kumagai, T. Hosaka, T. Kameda and T. Yoshioka, Pyrolysis and hydrolysis behaviors during steam pyrolysis of polyimide, *J. Anal. Appl. Pyrolysis*, 2016, **120**, 75–81.

5 *Research and Markets, Insights on the Polyimide Film Global Market to 2024 – Featuring DowDupont, SKC Kolon PI & Toray Industries Among Others*, **ResearchAndMarkets.com**, Business Wire (English), 2020.

6 Y. Cui, G. Li, H. Wu, S. Pang, Y. Zhuang, Z. Si, X. Zhang and P. Qin, Preparation and characterization of asymmetric Kapton membranes for gas separation, *React. Funct. Polym.*, 2023, **191**, 105667.
7 F. Huang, Y. Huang and Z. Pan, Depolymerization of ODPA/ODA Polyimide in a Fused Silica Capillary Reactor and Batch Autoclave Reactor from 320 to 350 °C in Hot Compressed Water, *Ind. Eng. Chem. Res.*, 2012, **51**(20), 7001–7006.
8 L. E. Stephans, A. Myles and R. R. Thomas, Kinetics of Alkaline Hydrolysis of a Polyimide Surface, *Langmuir*, 2000, **16**, 4706.
9 S. Kumagai, T. Hosaka, T. Kameda and T. Yoshioka, Steam Pyrolysis of Polyimides: Effects of Steam on Raw Material Recovery, *Environ. Sci. Technol.*, 2015, **49**(22), 13558–13565.
10 H. Liu, J. Gu, H. Fan, H. Yuan and Y. Wu, Thermal conversion performance, kinetic mechanism, and products of electric vehicle lithium battery diaphragms, *Energy Convers. Manage.*, 2023, **295**, 117612.
11 G. D. Mumbach, J. L. F. Alves, J. C. G. Da Silva, R. F. De Sena, C. Marangoni, R. A. F. Machado and A. Bolzan, Thermal investigation of plastic solid waste pyrolysis via the deconvolution technique using the asymmetric double sigmoidal function: Determination of the kinetic triplet, thermodynamic parameters, thermal lifetime and pyrolytic oil composition for clean energy recovery, *Energy Convers. Manage.*, 2019, **200**, 112031.
12 N. Leeabai, S. Suzuki, Q. Jiang, D. Dilixiati and F. Takahashi, The effects of setting conditions of trash bins on waste collection performance and waste separation behaviors; distance from walking path, separated setting, and arrangements, *Waste Manage.*, 2019, **94**, 58–67.
13 Y. Qiao, B. Wang, P. Zong, Y. Tian, F. Xu, D. Li, F. Li and Y. Tian, Thermal behavior, kinetics and fast pyrolysis characteristics of palm oil: Analytical TG-FTIR and Py-GC/MS study, *Energy Convers. Manage.*, 2019, **199**, 111964.
14 Y. X. Shen, M. S. Zhan, K. Wang, X. H. Li and P. C. Pan, The pyrolysis behaviors of polyimide foam derived from 3,3′,4,4′-benzophenone tetracarboxylic dianhydride/4,4′-oxydianiline, *J. Appl. Polym. Sci.*, 2010, **115**, 1680.
15 H. Hatori, Y. Yamada, M. Shiraishi, M. Yoshihara and T. Kimura, The mechanism of polyimide pyrolysis in the early stage, *Carbon*, 1996, **34**, 201.
16 N. Ohta, Y. Nishi, T. Morishita, T. Tojo and M. Inagaki, Preparation of microporous carbon films from fluorinated aromatic polyimides, *Carbon*, 2008, **46**, 1350.
17 M. Inagaki, T. Morishita, A. Kuno, T. Kito, M. Hirano, T. Suwa and K. Kusakawa, Carbon foams prepared from polyimide using urethane foam template, *Carbon*, 2004, **42**, 497.
18 Y. Xiao, Y. Dai, T.-S. Chung and M. D. Guiver, Effects of Brominating Matrimid Polyimide on the Physical and Gas Transport Properties of Derived Carbon Membranes, *Macromolecules*, 2005, **38**(24), 10042–10049.
19 G. F. L. Ehlers, K. R. Fisch and W. R. Powell, Thermal degradation of polymers with phenylene units in the chain. IV. Aromatic polyamides and polyimides, *J. Polym. Sci., Part A: Polym. Chem.*, 1970, **8**(12), 3511–3527.
20 P. R. Hondred, S. Yoon, N. Bowler, E. Moukhina and M. R. Kessler, Degradation kinetics of polyimide film, *High Perform. Polym.*, 2011, **23**, 335–342.
21 G. Li, Z. Si, S. Yang, T. Xue, J. Baeyens and P. Qin, Fast layer-by-layer assembly of PDMS for boosting the gas separation of P84 membranes, *Chem. Eng. Sci.*, 2022, **253**, 117588.
22 S. Vyazovkin, A. K. Burnham, J. M. Criado, L. A. Pérez-Maqueda, C. Popescu and N. Sbirrazzuoli, ICTAC Kinetics Committee recommendations for performing kinetic computations on thermal analysis data, *Thermochim. Acta*, 2011, **520**(1–2), 1–19.
23 S. Yousef, J. Eimontas, N. Striūgas, A. Mohamed and M. Ali Abdelnaby, Pyrolysis kinetic behavior and TG-FTIR-GC–MS analysis of end-life ultrafiltration polymer nanocomposite membranes, *Chem. Eng. J.*, 2022, **428**, 131181.
24 S. Yousef, J. Eimontas, N. Striūgas, K. Zakarauskas, M. Praspaliauskas and M. A. Abdelnaby, Pyrolysis kinetic behavior and TG-FTIR-GC–MS analysis of metallised food packaging plastics, *Fuel*, 2020, **282**, 118737.
25 Y. Wen, Z. Shi, S. Wang, W. Mu, P. G. Jönsson and W. Yang, Pyrolysis of raw and anaerobically digested organic fractions of municipal solid waste: Kinetics, thermodynamics, and product characterization, *Chem. Eng. J.*, 2021, **415**, 129064.
26 D. Irmak Aslan, P. Parthasarathy, J. L. Goldfarb and S. Ceylan, Pyrolysis reaction models of waste tires: Application of Master-Plots method for energy conversion via devolatilization, *Waste Manage.*, 2017, **68**, 405–411.
27 Y. Xu, C. Chen and J. Li, Experimental study on physical properties and pervaporation performances of polyimide membranes, *Chem. Eng. Sci.*, 2007, **62**(9), 2466–2473.
28 Y. Li, R. Yang, R. Zhang, B. Cao and P. Li, Preparation of Thermally Imidized Polyimide Nanofiltration Membranes with Macrovoid-Free Structures, *Ind. Eng. Chem. Res.*, 2020, **59**(31), 14096–14105.
29 J. Wang, X. Zhao, E. B. Berda, C. Chen, K. Wang, S. Chen, B. Zou, B. Liu, Q. Zhou, F. Li and D. Chao, The elastic properties and piezochromism of polyimide films under high pressure, *Polymer*, 2016, **90**, 1–8.
30 F. Y. Tsai, T. Blanton, D. R. Harding and S. Chen, Temperature dependence of the properties of vapor-deposited polyimide, *J. Appl. Phys.*, 2003, **93**, 3760–3764.
31 T. J. Shin, B. Lee, H. S. Youn, K.-B. Lee and M. Ree, Time-Resolved Synchrotron X-ray Diffraction and Infrared Spectroscopic Studies of Imidization and Structural Evolution in a Microscaled Film of PMDA-3,4'-ODA Poly(amic acid), *Langmuir*, 2001, **17**(25), 7842–7850.
32 Y. Isono, A. Yoshida, Y. Hishiyama and Y. Kaburagi, Carbonization and graphitization of shavings filed away from Kapton, *Carbon*, 2004, **42**(8–9), 1799–1805.
33 F. E. Elbakoush, Q. U. Khan, M. Ullah, A. Ullah, A. U. Khan, J. Khan and A. Iftikhar, Characterization and Thermal Degradation Study of Carbonization the Polyimide (PMDA/ODA)/Fe Composite Films, *Trans. Electr. Electron. Mater.*, 2021, **22**, 843–850.
34 R. Li, C. Li, S. He, M. Di and D. Yang, Damage effect of keV proton irradiation on aluminized Kapton film, *Radiat. Phys. Chem.*, 2008, **77**(4), 482–489.

35 M. A. Nahil and P. T. Williams, Surface chemistry and porosity of nitrogen-containing activated carbons produced from acrylic textile waste, *Chem. Eng. J.*, 2012, **184**, 228–237.
36 P. S. Wang, T. N. Wittberg and J. D. Wolf, A characterization of Kapton polyimide by X-ray photoelectron spectroscopy and energy dispersive spectroscopy, *J. Mater. Sci.*, 1988, **23**(11), 3987–3991.
37 H. Konno, T. Nakahashi and M. Inagaki, State analysis of nitrogen in carbon film derived from polyimide Kapton, *Carbon*, 1997, **35**(5), 669–674.
38 H. Hantsche, High resolution XPS of organic polymers, the scienta ESCA300 database. By G. Beamson and D. Briggs, Wiley, Chichester 1992, 295 pp., hardcover, £ 65.00, ISBN 0-471-93592-1, *Adv. Mater.*, 1993, **5**(10), 778.
39 A. K. Hołda and I. F. J. Vankelecom, Integrally skinned PSf-based SRNF-membranes prepared via phase inversion—Part A: Influence of high molecular weight additives, *J. Membr. Sci.*, 2014, **450**, 512–521.
40 M. A. Aroon, A. F. Ismail, M. M. Montazer-Rahmati and T. Matsuura, Morphology and permeation properties of polysulfone membranes for gas separation: Effects of non-solvent additives and co-solvent, *Sep. Purif. Technol.*, 2010, **72**(2), 194–202.
41 Y. Cui, G. Li, H. Wu, S. Pang, Y. Zhuang, Z. Si, X. Zhang and P. Qin, Preparation and characterization of asymmetric Kapton membranes for gas separation, *React. Funct. Polym.*, 2023, **191**, 105667.
42 S. P. Deshmukh and K. Li, Effect of ethanol composition in water coagulation bath on morphology of PVDF hollow fibre membranes, *J. Membr. Sci.*, 1998, **150**(1), 75–85.
43 F. Riedewald, Y. Patel, E. Wilson, S. Santos and M. Sousa-Gallagher, Economic assessment of a 40,000 t/y mixed plastic waste pyrolysis plant using direct heat treatment with molten metal: A case study of a plant located in Belgium, *Waste Manage.*, 2021, **120**, 698–707.
44 H. Ren, J. Jin, J. Hu and H. Liu, Affinity between Metal–Organic Frameworks and Polyimides in Asymmetric Mixed Matrix Membranes for Gas Separations, *Ind. Eng. Chem. Res.*, 2012, **51**(30), 10156–10164.
45 E. P. Favvas, S. K. Papageorgiou, J. W. Nolan, K. L. Stefanopoulos and A. C. Mitropoulos, Effect of air gap on gas permeance/selectivity performance of BTDA-TDI/MDI copolyimide hollow fiber membranes, *J. Appl. Polym. Sci.*, 2013, **130**(6), 4490–4499.
46 S. N. M. Kamal, C. P. Leo, A. L. Ahmad and M. U. M. Junaidi, Effects of THF as cosolvent in the preparation of polydimethylsiloxane/polyethersulfone membrane for gas separation, *Polym. Eng. Sci.*, 2014, **54**(9), 2177–2186.
47 Y. Qiu, J. Ren, D. Zhao, H. Li, K. Hua, X. Li and M. Deng, Blend membranes of poly(amide-6-b-ethylene oxide)/[Emim][PF6] for CO_2 separation, *Sep. Purif. Technol.*, 2017, **179**, 309–319.
48 A. B. Yumru, M. Safak Boroglu and I. Boz, ZIF-11/Matrimid® mixed matrix membranes for efficient CO_2, CH_4, and H_2 separations, *Greenhouse Gases: Sci. Technol.*, 2018, **8**(3), 529–541.
49 A. A. Emerenciano, R. M. Do Nascimento, A. P. C. Barbosa, K. Ran, W. A. Meulenberg and J. Gonzalez-Julian, Ti3C2 MXene Membranes for Gas Separation: Influence of Heat Treatment Conditions on D-Spacing and Surface Functionalization, *Membranes*, 2022, **12**(10), 1025.
50 Y.-g. Yan, Z.-j. Mao, J.-j. Luo, R.-p. Du and J.-x. Lin, Simultaneous removal of SO_2, NO_x and Hg0 by O_3 oxidation integrated with bio-charcoal adsorption, *J. Fuel Chem. Technol.*, 2020, **48**(12), 1452–1460.
51 J. Eimontas, S. Yousef, N. Striūgas and M. A. Abdelnaby, Catalytic pyrolysis kinetic behaviour and TG-FTIR-GC–MS analysis of waste fishing nets over ZSM-5 zeolite catalyst for caprolactam recovery, *Renewable Energy*, 2021, **179**, 1385–1403.
52 X. Peng, X. Ma, Y. Lin, Z. Guo, S. Hu, X. Ning, Y. Cao and Y. Zhang, Co-pyrolysis between microalgae and textile dyeing sludge by TG–FTIR: Kinetics and products, *Energy Convers. Manage.*, 2015, **100**, 391–402.
53 Y. X. Shen, M. S. Zhan, K. Wang, X. H. Li and P. C. Pan, The pyrolysis behaviors of polyimide foam derived from 3,3′,4,4′-benzophenone tetracarboxylic dianhydride/4,4′-oxydianiline, *J. Appl. Polym. Sci.*, 2009, **115**(3), 1680–1687.
54 W.-J. Chou, C.-C. Wang and C.-Y. Chen, Thermal behaviors of polyimide with plasma-modified carbon nanotubes, *Polym. Degrad. Stab.*, 2008, **93**(3), 745–752.
55 E. Pretsch, P. Bühlmann and M. Badertscher, *IR Spectroscopy [M]. Structure Determination of Organic Compounds: Tables of Spectral Data*, Berlin, Heidelberg, Springer Berlin Heidelberg, 2009, pp. 1–67.
56 G. Montaudo, C. Puglisi, J. W. De Leeuw, W. Hartgers, K. Kishore and K. Ganesh, Thermal Degradation Processes in Poly(xylylene sulfides) Investigated by Comparative Direct Pyrolysis MS and Flash Pyrolysis GC/MS Experiments, *Macromolecules*, 1996, **29**(20), 6466–6474.
57 C. Puglisi, F. Samperi, S. Carroccio and G. Montaudo, MALDI−TOF Investigation of Polymer Degradation. Pyrolysis of Poly(bisphenol A carbonate), *Macromolecules*, 1999, **32**(26), 8821–8828.
58 S. D. Bruck, Thermal degradation of an aromatic polypyromellitimide in air and vacuum II-The effects of impurities and the nature of degradation products, *Polymer*, 1965, **6**, 49.
59 J. Żurakowska-Orszàgh and T. Chreptowicz, Thermal degradation of polyimides—II: Mechanism of carbon dioxide formation during thermal degradation, *Eur. Polym. J.*, 1981, **17**(8), 877–880.
60 S. Tang, G. Tan, J. Liang, O. Li, W. Xuan and Z. Li, Key element course-tracked copyrolysis of sewage sludge and biomass for resource recovery and pollution control through kinetic and thermodynamic insights, *Energy Convers. Manage.*, 2023, **280**, 116830.
61 X. Zhu, K. Li, L. Zhang, X. Wu and X. Zhu, Synergistic effects on thermochemical behaviors of co-pyrolysis between bio-oil distillation residue and bituminous coal, *Energy Convers. Manage.*, 2017, **151**, 209–215.

62 T. Nonobe, S. Tsuge, H. Ohtani, T. Kitayama and K. Hatada, Stereoregularity of Poly(methyl methacrylate)s Studied by Pyrolysis–Gas Chromatography/Mass Spectroscopy, *Macromolecules*, 1997, **30**(17), 4891–4896.

63 H. Zhang, R. J. Farris and P. R. Westmoreland, Low Flammability and Thermal Decomposition Behavior of Poly(3,3'-dihydroxybiphenylisophthalamide) and Its Derivatives, *Macromolecules*, 2003, **36**(11), 3944–3954.

64 G. F. L. Ehlers, K. R. Fisch and W. R. Powell, Thermal degradation of polymers with phenylene units in the chain. II. Sulfur-containing polyarylenes, *J. Polym. Sci., Part A: Polym. Chem.*, 1969, **7**(10), 2955–2967.

65 D. Trache, A. Abdelaziz and B. Siouani, A simple and linear isoconversional method to determine the pre-exponential factors and the mathematical reaction mechanism functions, *J. Therm. Anal. Calorim.*, 2017, **128**(1), 335–348.

66 S. Lv, Y. Zhang and H. Tan, Thermal and thermo-oxidative degradation kinetics and characteristics of poly (lactic acid) and its composites, *Waste Manage.*, 2019, **87**, 335–344.

67 Y.-L. Liu, C.-S. Wu, Y.-S. Chiu and W.-H. Ho, Preparation, thermal properties, and flame retardance of epoxy–silica hybrid resins, *J. Polym. Sci., Part A: Polym. Chem.*, 2003, **41**(15), 2354–2367.

68 C. Sun, X. Chen, D. Zheng, W. Yao, H. Tan, Y. Zhang and S. Liu, Exploring the synergetic effects of the major components of biomass additives in the pyrolysis of polylactic acid, *Green Chem.*, 2021, **23**(22), 9014–9023.

69 Y. Liu, Y. Song, J. Fu, W. Ao, A. Ali Siyal, C. Zhou, C. Liu, M. Yu, Y. Zhang, J. Dai and X. Bi, Co-pyrolysis of sewage sludge and lignocellulosic biomass: Synergistic effects on products characteristics and kinetics, *Energy Convers. Manage.*, 2022, **268**, 116061.

70 M. Majid, B. L. F. Chin, Z. A. Jawad, Y. H. Chai, M. K. Lam, S. Yusup and K. W. Cheah, Particle swarm optimization and global sensitivity analysis for catalytic co-pyrolysis of Chlorella vulgaris and plastic waste mixtures, *Bioresour. Technol.*, 2021, **329**, 124874.

71 M. Majid, B. L. F. Chin, Z. A. Jawad, Y. H. Chai, M. K. Lam, S. Yusup and K. W. Cheah, Particle swarm optimization and global sensitivity analysis for catalytic co-pyrolysis of Chlorella vulgaris and plastic waste mixtures, *Fuel*, 2023, **331**, 125735.

72 J. Yan, Q. Yang, L. Zhang, Z. Lei, Z.-K. Li, Z. Wang, S. Ren, S. Kang and H. Shui, Investigation of kinetic and thermodynamic parameters of coal pyrolysis with model-free fitting methods, *Carbon Resour. Convers.*, 2020, **3**, 173–181.

73 S. A. El-Sayed and M. E. Mostafa, Pyrolysis and co-pyrolysis of Egyptian olive pomace, sawdust, and their blends: Thermal decomposition, kinetics, synergistic effect, and thermodynamic analysis, *J. Cleaner Prod.*, 2023, **401**, 136772.

74 Y. Xu and B. Chen, Investigation of thermodynamic parameters in the pyrolysis conversion of biomass and manure to biochars using thermogravimetric analysis, *Bioresour. Technol.*, 2013, **146**, 485–493.

75 G. Gözke, Kinetic and thermodynamic analyses based on thermogravimetric pyrolysis of watermelon seed by isoconversional and master plots methods, *Renewable Energy*, 2022, **201**, 916–927.

76 Y. Qu, A. Li, D. Wang, L. Zhang and G. Ji, Kinetic study of the effect of in-situ mineral solids on pyrolysis process of oil sludge, *Chem. Eng. J.*, 2019, **374**, 338–346.